The Influence of Non-Sinusoidal Inductance on Saliency-Based Position Estimation for Permanent Magnet Machine

KUO-YUAN HUNG[ID][1], **(Student Member, IEEE), PO-HUAN CHOU**[2],
NAI-WEN LIU[ID][1], **(Student Member, IEEE), YU-LIANG HSU**[ID][3], **(Member, IEEE),**
AND SHIH-CHIN YANG[ID][1], **(Senior Member, IEEE)**

[1]Department of Mechanical Engineering, National Taiwan University, Taipei 10617, Taiwan
[2]Industrial Technology Research Institute, Hsinchu 31057, Taiwan
[3]Department of Mechanical and Electro-Mechanical Engineering, National Sun Yat-sen University, Kaohsiung 804, Taiwan

Corresponding author: Shih-Chin Yang (scy99@ ntu.edu.tw)

ABSTRACT This paper analyzes the influence of non-sinusoidal inductance distortion on the saliency-based position estimation for the permanent magnet (PM) machines. Because of the high-power-density design of PM machines, the flux saturation usually causes the inductance self-saturation, inductance cross-saturation, and most importantly, secondary inductance harmonics. This paper fully investigates the saturation effect on saliency-based drives. Analytical model for the position estimation with saturated inductance is developed to understand the stability of saliency-based drive. It is confirmed that the saturation effect deviates the estimated flux position from actual rotor position. These estimation errors are critical for the saliency-based drive especially under load. This paper defines the feasible estimation region for PM machines with saturated and non-sinusoidal inductances. Considering the position estimation errors due to the saturated and non-sinusoidal inductance, the typical maximum torque per amp (MTPA) current trajectory based on the encoder-based control system should be modified especially for the IPM machines at full load. For the machines where the saturation condition is unknown, q-axis current without negative d-axis current is suggested to maintain control stability while the torque reduction is resultant. By contrast, the modified current trajectory could also be designed once the saturation reflected position estimation errors could be obtained. Finite element analysis (FEA) with inverter co-simulation is used to investigate the inductance distortion at various loads. A 6 kW IPM machine prototype with highly non-sinusoidal inductance is tested for the experimental verification.

INDEX TERMS Sensorless machine drive, saliency-based position estimation, and high-frequency voltage injection.

I. INTRODUCTION

High-performance permanent magnet machine drive requires instantaneous position information to realize field-oriented control (FOC). For conventional sensor-based drives, separated position sensors, e.g. encoders and resolvers, are attached to obtain the instantaneous rotor position. However, the installation of position sensors degrades the FOC drive reliability [1]. Elimination of separated position sensors by using the position information from the machine itself

The associate editor coordinating the review of this manuscript and approving it for publication was Paolo Giangrande[ID].

(self-sensing) has become a promising solution. Considering the position sensorless drive at zero and low speed, the rotor position can be estimated through the spatial signal in machine inductances with high frequency (HF) AC voltage persistent injection [2]–[4].

Unfortunately, the position information provided by the machine inductance results in signal distortions due to the saturation. These saturation reflected attributes include 1) the saliency magnitude reduction [5], 2) cross-saturation (mutual-coupling) between rotor d-axis and q-axis [6], and 3) secondary inductance harmonics [7], [8]. It is important that the influence of saturation on position estimation

increases as the load increases. They limit the saliency-based drive at full load, blocking them from the progress into industrial products.

The flux saturation firstly reduces the saliency magnitude, e.g. self-saturation, leading to the drive stability issue at high load. Considering the machine control with maximum torque per ampere (MTPA), q-axis inductance L_q decreases as the load increases. For IPM machines with saliency whereby q-axis $L_q > d$-axis inductance L_d, the saliency eventually reduces to zero which is not useful for position estimation. In [5], the rotor barrier is designed to reduce the load dependent saturation on L_q. Both the concentrated and distributed windings are also compared in [9] under the same IPM machine topology. It is reported that distributed windings lead to the minor saturation on L_q comparing to concentrated windings. Besides, an IPM machine with reverse saliency is proposed in [10]. Because of reverse saliency whereby $L_d > L_q$, the saliency increases as the load increases, leading to the better estimation performance at full load. However, the torque might reduce since the reverse saliency $L_d > L_q$ is not as high as conventional saliency $L_q > L_d$.

In addition to inductance self-saturation, the flux saturation also causes the cross-saturation between orthogonal d- and q-axis. Under this effect, the saliency estimated flux position is no longer aligned with actual rotor position [6]. It is noted that d-q cross-saturation results in the constant offset on the position estimation. The saliency-based drive fails when the position offset is larger than 45 deg. In [11], the position offset is compensated based on one-dimensional look-up table (LUT). The offset compensation is directly added dependent on the load condition. However, in [12] and [13], it is reported that d-q mutual-coupling is influenced by both torque load and rotor position. Under this effect, two-dimensional LUT is proposed to improve the offset compensation. Instead of LUT, the stator windings, tooth shape and rotor structure can be designed to mitigate d-q cross-saturation [14], [15].

Instead of self- and cross-saturation, the saturation also increases secondary harmonics in machine inductances. Considering the ideally sinusoidal-distributed inductance in IPM machines, only the 2nd-order spatial harmonic in the stator-referred stationary frame is resultant. However, once the saturation occurs, the stator-referred inductance contains additional 4th-, 6th-, 8th-order, etc. harmonics. As reported in [16], these inductance harmonics lead to periodic position estimation errors. Consequently, the position estimation fails once secondary harmonic magnitudes are higher than the fundamental magnitude. In [7], the adaptive decoupling is applied to remove these harmonics if harmonic magnitudes and phases are well-known. In addition, neural network compensation is developed through the database training with a sensor-based drive [17]. In [18], secondary saliency harmonics can be improved by the tracking of multiple saliency harmonics. Besides in [19], the saturation reflected inductance harmonics have more influence on the zero-sequence voltage measurement than saliency current measurement under the same voltage injection. For the compensation of these inductance harmonics, all saliency harmonic magnitudes should be known on the estimated IPM machine.

This paper improves the saliency-based position estimation for the IPM machine with saturation reflected non-sinusoidal inductance. Although the influence of inductance cross-saturation and secondary harmonics have been reported on saliency-based drives, very few researches are related to the root causes of inductance distortion on PM machines. To fully investigate the saturation effect on saliency-based drives, an analytical model of the position estimation with saturated inductance is developed. For an IPM machine with considerable inductance harmonics, it is not possible to realize the saliency-based drive with conventional MTPA current trajectory. In order to investigate the drive stability, the inductance saturation property is carefully investigated to identify the most efficient operating condition. Two modified MTPA d-q current trajectories are proposed to maintain the saliency-based drive stability under load. For IPM machines where the saturation condition is unknown, q-axis current without negative d-axis current is suggested to maintain MTPA control stability. By contrast, the modified current trajectory can also be designed once the saturation reflected position estimation errors can be obtained. Although the efficiency is not compatible with encoder-based drive, the saliency-based drive can be maintained for machines with non-sinusoidal inductances. A 6 kW IPM machine is used for the experimental verification.

II. SALIENCY-BASED POSITION ESTIMATION
This section analyzes the inductance saturation on the saliency-based position estimation. The saturation results in the saliency ratio reduction, d-q cross-saturation and secondary harmonics. Analytical models are proposed to predict the corresponding estimations errors. Position compensation methods are then developed based on these analytical models.

A. SATURATION REFLECTED SALIENCY RATIO REDUCTION
For simplicity, an IPM machine with the linear flux distribution is firstly analyzed. Considering the ideal model, the d-q inductances matrix L_{dq} and α-β inductances matrix $L_{\alpha\beta}$ are respectively derived by (1) and (2).

$$\mathbf{L}_{dq} = \begin{bmatrix} L_{dd} & 0 \\ 0 & L_{qq} \end{bmatrix} = \begin{bmatrix} \Sigma L - \Delta L & 0 \\ 0 & \Sigma L + \Delta L \end{bmatrix} \quad (1)$$

$$\begin{aligned} \mathbf{L}_{\alpha\beta} &= \begin{bmatrix} L_{\alpha\alpha} & L_{\alpha\beta} \\ L_{\alpha\beta} & L_{\beta\beta} \end{bmatrix} \\ &= \begin{bmatrix} \sum L - \Delta L \cos(2\theta_e) & -\Delta L \sin(2\theta_e) \\ -\Delta L \sin(2\theta_e) & \sum L + \Delta L \cos(2\theta_e) \end{bmatrix} \end{aligned} \quad (2)$$

where $\Sigma L (L_{qq} + L_{dd})/2$ and $\Delta L (L_{qq} - L_{dd})/2$ are the average and difference inductance. In (2), θ_e is the rotor position with electrical angle. It is noted that $2\theta_e$ position information appears in $\mathbf{L}_{\alpha\beta}$ which is used for saliency-based position estimation.

However, considering the nonlinear property of magnetic materials, both self- and cross-saturation are resultant. Under

this effect, all inductances in $\mathbf{L}_{dq}$ and $\mathbf{L}_{\alpha\beta}$ decrease as load increases. Fig. 1 illustrates α-axis self-inductance $L_{\alpha\alpha}$ in (1) versus the rotor position.
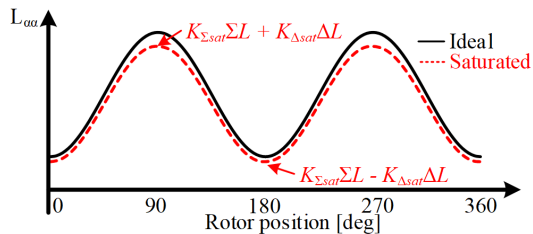
FIGURE 1. Illustration of the saturation reflected α-axis self-inductance versus rotor position in stator referred stationary frame.

For IPM machines, the saturation primarily locates at rotor ribs. It results in the considerable magnitude reduction on ΣL. In addition, load reflected q-axis current also causes the reduction on ΔL. Considering the self-inductance saturation, the inductance matrix $\mathbf{L}_{dq}$ in (1) and $\mathbf{L}_{\alpha\beta}$ in (2) should be modified by $\mathbf{L}_{dq1}$ in (3) and $\mathbf{L}_{\alpha\beta1}$ in (4), as shown at the bottom of the page, where $K_{\Sigma sat}$ and $K_{\Delta sat}$ are the coefficients smaller than 1 and dependent on machine topologies. $K_{\Sigma sat}$ and $K_{\Delta sat}$ are used to analyze the inductance magnitude reduction respectively for average inductance ΣL and difference inductance ΔL, as seen in Fig. 1. Considering the salient PM machine, the torque output consists of electromagnetic torque and reluctance torque. At low speed under constant torque region, the electromagnetic torque is dominated. In this case, i_q with current angle at 90 deg is larger than i_d at low speed with 0 deg angle. In order to provide sufficient i_q for electromagnetic torque production, the inductance reduction at 90 deg (q-axis) with $K_{\Sigma sat}\Sigma L + K_{\Delta sat}\Delta L$ is larger than that at 0 deg (d-axis) with $K_{\Sigma sat}\Sigma L - K_{\Delta sat}\Delta L$.

To implement the saliency-based position estimation, a HF rotating voltage $V_{\alpha\beta\_HF}$ shown in (5) is superimposed on the fundamental voltage to induce position dependent signal.

$$\mathbf{V}_{\alpha\beta\_HF} = \begin{bmatrix} v_{\alpha\_HF} \\ v_{\beta\_HF} \end{bmatrix} = \begin{bmatrix} v_c \cos(-\omega_c t) \\ v_c \sin(-\omega_c t) \end{bmatrix}$$
$$= \frac{d}{dt}\left(\mathbf{L}_{\alpha\beta1} \cdot \mathbf{I}_{\alpha\beta1\_HF}\right) \quad (5)$$

where v_c is the injection voltage magnitude and ω_c is the injection frequency. In this paper, the rotating voltage is selected for the purpose to demonstrate the saturation reflected saliency distortion. Considering the influence of inverter non-linearity, other advanced HF voltages, e.g. square-wave, can be selected to reduce the deadtime effect.

By superimposing the HF voltage $V_{\alpha\beta\_HF}$, the inductive voltage drop is dominant at low speed since the EMF voltage is sufficiently low. The resulting HF current can be shown by

$$\mathbf{I}_{\alpha\beta1\_HF}$$
$$= \begin{bmatrix} i_{\alpha1\_HF} \\ i_{\beta1\_HF} \end{bmatrix} = \frac{v_c}{\omega_c} \frac{1}{(K_{\Sigma sat}\Sigma L)^2 - (K_{\Delta sat}\Delta L)^2}$$
$$\cdot \begin{bmatrix} K_{\Sigma sat}\Sigma L \sin(\omega_c t) + K_{\Delta sat}\Delta L \sin(-\omega_c t + 2\theta_e) \\ K_{\Sigma sat}\Sigma L \cos(\omega_c t) + K_{\Delta sat}\Delta L \cos(-\omega_c t + 2\theta_e) \end{bmatrix}$$
$$(6)$$

A $2\theta_e$ saliency position signal occurs on both α- and β-axis HF current $i_{\alpha1\_HF}$ and $i_{\beta1\_HF}$. Thus, the rotor position can be estimated by extracting $2\theta_e$ from and. However, the magnitude of $2\theta_e$ reflected signal is proportional to the saliency, $K_{\Sigma sat}\Delta L$. Considering the saturation, $K_{\Delta sat}$ decreases and eventually, $2\theta_e$ signal disappears.

Based on the model in (6), Fig. 2 illustrates the influence of saturation on the saliency image distortion. Here, the saliency image is represented by the current trajectory of β-axis current $i_{\beta1\_HF}$ versus α-axis $i_{\alpha1\_HF}$ in (6). In this figure, the injection frequency ω_c is designed at 1KHz and the rotor positions θ_e are assumed respectively at 0 and 90 deg for the saliency image comparison.

Four different conditions are respectively analyzed. They are (a) no saturation at no load ($K_{\Sigma sat} = K_{\Delta sat} = 1$), (b) the saliency reduction at 40% load ($K_{\Sigma sat} = 0.83$ and $K_{\Delta sat} = 0.5$), (c) the reduction at 85% load ($K_{\Sigma sat} = 0.67$ and $K_{\Delta sat} = 0$), and (d) reverse saliency at 120% load ($K_{\Sigma sat} = 0.60$ and $K_{\Delta sat} = -0.2$). In Fig. 2, both $K_{\Sigma sat}$ and $K_{\Delta sat}$ in (4) are selected based on the FEA simulation of test IPM machine with considerable inductance saturation. Detail explanation of this test IPM machine will be shown in section III and IV. The HF current trajectory at two different positions, $\theta_e = 0$ deg and 90 deg, are overlaid within a single plot to clearly illustrate the saliency image at different positions.

Considering Fig. 2(a) without the saturation, the HF current trajectory is equivalent to an ellipse where the minor- and major-axis are aligned respectively to $\theta_e + 0$ deg and $\theta_e + 90$ deg. The actual diameter of two axes can be obtained based on (6) by substituting the instantaneous θ_e. As seen in (6), the position signal proportional to ΔL results in the difference of two axes diameter. Under this effect, the diameter difference should be as high as possible in order to achieve a high signal-to-noise ratio (SNR) for the estimation. In Fig. 2 (a) at no load $K_{\Delta sat} = 1$, the rotor position can be estimated by identifying this diameter difference.

However, as saturation increases where $K_{\Delta sat} = 0.5$ in (b), the saliency image distorts from an ellipse to a circle. It is seen

$$\mathbf{L}_{dq1} = \begin{bmatrix} K_{\Sigma sat}\Sigma L - K_{\Delta sat}\Delta L & 0 \\ 0 & K_{\Sigma sat}\Sigma L + K_{\Delta sat}\Delta L \end{bmatrix} \quad (3)$$

$$\mathbf{L}_{\alpha\beta1} = \begin{bmatrix} K_{\Sigma sat}\Sigma L - K_{\Delta sat}\Delta L \cos(2\theta_e) & -K_{\Delta sat}\Delta L \sin(2\theta_e) \\ -K_{\Delta sat}\Delta L \sin(2\theta_e) & K_{\Sigma sat}\Sigma L + K_{\Delta sat}\Delta L \cos(2\theta_e) \end{bmatrix} \quad (4)$$
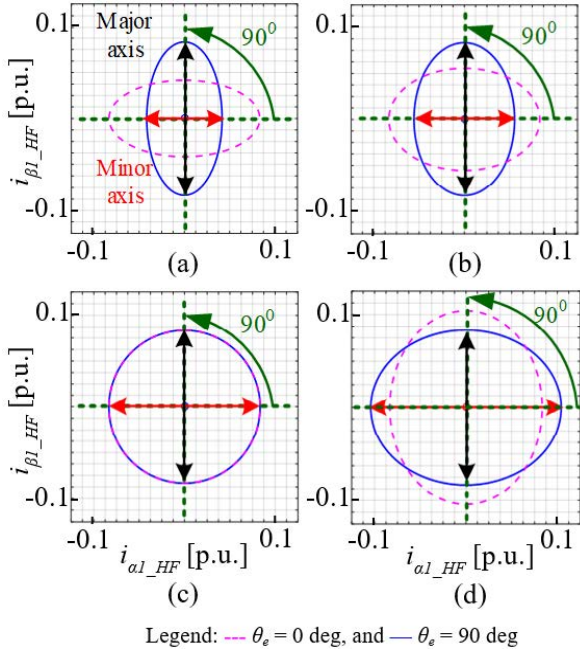
FIGURE 2. HF current trajectory of $i_{\beta1\_HF}$ versus the $i_{\alpha1\_HF}$ at 4 conditions: (a) no saturation at no load, (b) saliency reduction at 40% load, (c) no saliency at 85% load, and (d) reverse saliency at 120% load.

FIGURE 3. HF current trajectory of $i_{\beta2\_HF}$ versus the $i_{\alpha2\_HF}$ at 4 conditions: (a) $K_{\Sigma sat} = K_{\Delta sat} = 1$, (b) $K_{\Sigma sat} = 0.83$, $K_{\Delta sat} = 0.5$, (c) $K_{\Sigma sat} = 0.67$, $K_{\Delta sat} = 0$, and (d) $K_{\Sigma sat} = 0.60$, $K_{\Delta sat} = -0.20$ ($L_{dq} = 10\%$ of ΣL).

that the diameter difference decreases. At 85% load when $K_{\Delta sat} = 0$ in (c), the saliency image eventually becomes a circle. Because there is no difference between major- and minor-axis, it is not possible to obtain the $2\theta_e$ position signal in (6). Finally, in (d) when $K_{\Delta sat} < 0$, the circle changes back to ellipse due to the reverse saliency, $L_d > L_q$. In this case, the reverse saliency whereby $\Delta L < 0$ is appeared once q-axis inductance L_{qq} is fully saturated at full load. Under this effect, the position estimation results in 90 deg position offset because the major-axis is aligned with $\theta_e + 90$ deg, as demonstrated in Fig. 2(d).
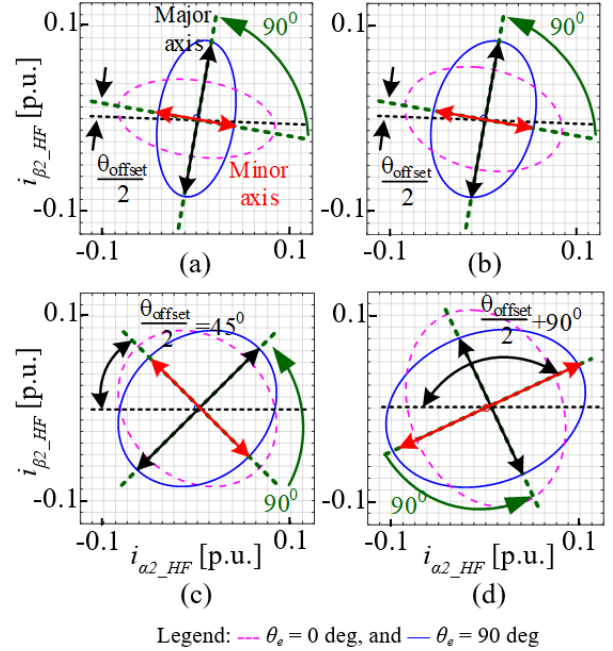
B. D-Q CROSS-SATURATION
In addition to saliency ratio reduction at part A, the saturation also causes the inductance phase offset as load increases. Under this effect, the estimated flux position is no longer aligned with the actual rotor position. On the basis, the cross-saturation can be modelled by additional non-diagonal elements in matrix $\mathbf{L}_{dq}$ from (1), as given by

$$\mathbf{L}_{dq2} = \begin{bmatrix} L_{dd} & L_{dq} \\ L_{dq} & L_{qq} \end{bmatrix} = \begin{bmatrix} \Sigma L - \Delta L & K_{cs} L_{dq} \\ K_{cs} L_{dq} & \Sigma L + \Delta L \end{bmatrix} \quad (7)$$

where $\mathbf{L}_{dq2}$ denotes d-q inductances matrix with cross-saturation, K_{cs} is a coefficient larger than 1 dependent on load conditions. Considering the cross-saturation, K_{cs} increases as the load increases [11]. Based on (7), the corresponding α-β inductances matrix $\mathbf{L}_{\alpha\beta2}$ is modified by

$$\mathbf{L}_{\alpha\beta2} = \begin{bmatrix} \cos(\theta_e) & \sin(\theta_e) \\ -\sin(\theta_e) & \cos(\theta_e) \end{bmatrix} \cdot \mathbf{L}_{dq2} \cdot \begin{bmatrix} \cos(\theta_e) & -\sin(\theta_e) \\ \sin(\theta_e) & \cos(\theta_e) \end{bmatrix}$$

$$= \mathbf{L}_{\alpha\beta1} + K_{cs} \begin{bmatrix} L_{dq}\sin(2\theta_e) & L_{dq}\cos(2\theta_e) \\ L_{dq}\cos(2\theta_e) & -L_{dq}\sin(2\theta_e) \end{bmatrix} \quad (8)$$

By combining the influence of both self-inductance saturation at part A and cross-saturation at part B, the injection induced HF current can be extended from (6) to (9).

$$\mathbf{I}_{\alpha\beta2\_HF}$$
$$= \begin{bmatrix} i_{\alpha2\_HF} \\ i_{\beta2\_HF} \end{bmatrix}$$
$$= \frac{v_c}{\omega_c} \left(\frac{(K_{\Sigma sat}\Sigma L)}{(K_{\Sigma sat}\Sigma L)^2 - (K_{\Delta sat}\Delta L)^2 - (K_{cs}L_{dq})^2} \begin{bmatrix} \sin(\omega_c t) \\ \cos(\omega_c t) \end{bmatrix} \right.$$
$$+ \frac{\sqrt{(K_{\Delta sat}\Delta L)^2 + (K_{sc}L_{dq})^2}}{(K_{\Sigma sat}\Sigma L)^2 - (K_{\Delta sat}\Delta L)^2 - (K_{cs}L_{dq})^2}$$
$$\times \left. \begin{bmatrix} \sin(-\omega_c t + 2\theta_e - 2\theta_{offset}) \\ \cos(-\omega_c t + 2\theta_e - 2\theta_{offset}) \end{bmatrix} \right) \quad (9)$$

where $\theta_{offset} = \tan^{-1}\left[(K_{sc}L_{dq})/(K_{\Delta sat}\Delta L) \right]$ is dependent on the ratio of $L_{dq}/\Delta L$.

Comparing HF current between (6) and (9), a position offset θ_{offset} is resultant due to cross-saturation.

Fig. 3 illustrates the saliency image versus under same conditions in Fig. 2 while the cross-saturation is included whereby $L_{dq} = 0.1 \Sigma L$. As seen from Fig. 3(a) and (b), saliency images are similar to the cases in Fig. 2.

However, the diameter difference between minor- and major-axis is slightly longer due to additional component from L_{dq}, as seen from the nominator from the last equation in (9). In addition, a visible offset occurs on two diagonal

axes. Because of cross-saturation, this offset is equivalent to $\theta_{offset}/2$. Fig. 3 (c) shows the image at no saliency where $\Delta L = 0$. As seen for $\mathbf{L}_{\alpha\beta2}$ in (8), cross-saturation L_{dq} term also contains the position signal. Under this effect, the saliency image with an ellipse pattern still results even when $\Delta L = 0$. The position estimation can still be implemented by estimating the diameter difference between two axes. At this time, θ_{offset} in (9) is equal to 90 deg by substituting $K_{\Delta sat}\Delta L = 0$. Finally, in Fig. 3(d) with reverse saliency, the position offset increases to $\theta_{offset}/2 + 90$ deg due to $L_q > L_d$.

Considering both the saturation reflected saliency reduction and cross-saturation, the position signal eventually disappears once $L_{dq} = \Delta L = 0$. This operating point is defined by the critical point for the saliency-based drive [5]. However, the discussion in [5] is under the sinusoidal inductance assumption without secondary harmonics. At next part, the influence of secondary inductance harmonics on the position estimation will be analyzed. It is shown that the infeasible estimation region extends to multiple areas instead of single critical point.

C. SECONDARY INDUCTANCE HARMONICS
Instead of saliency reduction and cross-saturation, the saturation also causes secondary harmonics on the sinusoidal inductance. In order to analyze inductance harmonics with various harmonics, a general form of *d-q* inductances matrix $\mathbf{L}_{dq\_G}$ is developed in (10), as shown at the bottom of the page. In (10), both self-inductances L_{dd_G} and L_{qq_G}

as well as mutual-inductance L_{dq_G} all contain $6^{\text{th}-}$ order spatial harmonics with respect to their corresponding angle offsets, $\theta_{dd,h'}, \theta_{qq,h'}$ and $\theta_{dq,h'}$. In addition, $L_{dd,0}, L_{qq,0}$ and $L_{dq,0}$ represent DC components of L_{dd_G}, L_{qq_G} and, L_{dq_G} and h' is the harmonic order from 1 to infinity. Considering the ideal machine without saturation, h' can be assumed by zero, as originally seen in (1). According to the proposed matrix L_{dq_G} in (10), ΔL can be represented as (11), shown at the bottom of the page With the *d-q* inductances matrix $\mathbf{L}_{dq\_G}$ in (10), the general form of α-β inductances matrix $\mathbf{L}_{\alpha\beta\_G}$ can be derived in (12), as shown at the bottom of the page, based on the frame transformation similar to (8), where

$$\Delta L_0 = \frac{L_{qq,0} - L_{dd,0}}{2}$$

$$\Delta L_{h'} = \frac{\sqrt{L_{qq,h'}^2 + L_{dd,h'}^2 - 2L_{qq,h'}L_{dd,h'}\cos(\theta_{qq,h'} - \theta_{dd,h'})}}{2}$$

$$\theta_{\Delta h'} = \tan^{-1}\left[\frac{L_{qq,h'}\sin(\theta_{qq,h'}) - L_{dd,h'}\sin(\theta_{dd,h'})}{L_{qq,h'}\cos(\theta_{qq,h'}) - L_{dd,h'}\cos(\theta_{dd,h'})}\right]$$

Since different inductance harmonics are cross-coupled during the transformation, only the secondary harmonic of h'=1 is considered in $\mathbf{L}_{\alpha\beta\_G}$ for simplicity. It is given by (12) In (12), both 4th- and 8th- order harmonic are resultant due to a saturation reflected 6th-order inductance harmonic in L_{dq_G}. By injecting a HF rotating voltage $\mathbf{V}_{\alpha\beta\_HF}$ in (5), the HF $\mathbf{I}_{\alpha\beta G\_HF}$ current with the influence of inductance

$$
\begin{aligned}
\mathbf{L}_{dq\_G} &= \begin{bmatrix} L_{dd\_G} & L_{dq\_G} \\ L_{dq\_G} & L_{qq\_G} \end{bmatrix} \\
&= \begin{bmatrix} L_{dd,0} + \sum_{h'=1}^{\infty} L_{dd,h'}\cos(6h'\theta_e + \theta_{dd,h'}) & L_{dq,0} + \sum_{h'=1}^{\infty} L_{dq,h'}\sin(6h'\theta_e + \theta_{dq,h'}) \\ L_{dq,0} + \sum_{h'=1}^{\infty} L_{dq,h'}\sin(6h'\theta_e + \theta_{dq,h'}) & L_{qq,0} + \sum_{h'=1}^{\infty} L_{qq,h'}\cos(6h'\theta_e + \theta_{qq,h'}) \end{bmatrix}
\end{aligned}
\tag{10}
$$

$$
\begin{aligned}
\Delta L &= \frac{L_{qq\_G} - L_{dd\_G}}{2} \\
&= \frac{L_{qq,0} - L_{dd,0}}{2} + \sum_{h'=1}^{\infty} \frac{L_{qq,h'}\cos(6h'\theta_e + \theta_{qq,h'}) - L_{dd,h'}\cos(6h'\theta_e + \theta_{dd,h'})}{2} \\
&= \Delta L_0 + \sum_{h'=1}^{\infty} \Delta L_{h'}\cos(6h'\theta_e + \theta_{\Delta h'})
\end{aligned}
\tag{11}
$$

$$
\begin{aligned}
\mathbf{L}_{\alpha\beta\_G} &= \begin{bmatrix} \cos(\theta_e) & \sin(\theta_e) \\ -\sin(\theta_e) & \cos(\theta_e) \end{bmatrix} \cdot \mathbf{L}_{dq\_G} \cdot \begin{bmatrix} \cos(\theta_e) & -\sin(\theta_e) \\ \sin(\theta_e) & \cos(\theta_e) \end{bmatrix} \\
&= \begin{bmatrix} \sum L & 0 \\ 0 & \sum L \end{bmatrix} + \begin{bmatrix} -\Delta L\cos(2\theta_e) + L_{dq}\sin(2\theta_e) & -\Delta L\sin(2\theta_e) + L_{dq}\cos(2\theta_e) \\ -\Delta L\sin(2\theta_e) + L_{dq}\cos(2\theta_e) & \Delta L\cos(2\theta_e) - L_{dq}\sin(2\theta_e) \end{bmatrix} \\
&\quad + \begin{bmatrix} -\Delta L_1\cos(-4\theta_e + \theta_{\Delta 1}) + L_{dq,1}\sin(-4\theta_e + \theta_{\Delta 1}) & -\Delta L_1\sin(-4\theta_e + \theta_{\Delta 1}) + L_{dq,1}\cos(-4\theta_e + \theta_{\Delta 1}) \\ -\Delta L_1\sin(-4\theta_e + \theta_{\Delta 1}) + L_{dq,1}\cos(-4\theta_e + \theta_{\Delta 1}) & \Delta L_1\cos(-4\theta_e + \theta_{\Delta 1}) - L_{dq,1}\sin(-4\theta_e + \theta_{\Delta 1}) \end{bmatrix} \\
&\quad + \begin{bmatrix} -\Delta L_1\cos(8\theta_e - \theta_{\Delta 1}) + L_{dq,1}\sin(8\theta_e - \theta_{\Delta 1}) & -\Delta L_1\sin(8\theta_e - \theta_{\Delta 1}) + L_{dq,1}\cos(8\theta_e - \theta_{\Delta 1}) \\ -\Delta L_1\sin(8\theta_e - \theta_{\Delta 1}) + L_{dq,1}\cos(8\theta_e - \theta_{\Delta 1}) & \Delta L_1\cos(8\theta_e - \theta_{\Delta 1}) - L_{dq,1}\sin(8\theta_e - \theta_{\Delta 1}) \end{bmatrix}
\end{aligned}
\tag{12}
$$

secondary harmonic $h' = 1$ can be shown by (13).

$$\mathbf{I}_{\alpha\beta G\_HF} = \begin{bmatrix} i_{\alpha G\_HF} \\ i_{\beta G\_HF} \end{bmatrix} = |I_{\sum L}| \begin{bmatrix} \sin(\omega_c t) \\ \cos(\omega_c t) \end{bmatrix}$$

$$+ |I_{\Delta L}| \begin{bmatrix} \sin(-\omega_c t + 2\theta_e - 2\theta_{offset}) \\ \cos(-\omega_c t + 2\theta_e - 2\theta_{offset}) \end{bmatrix}$$

$$+ |I_{\Delta L1\_-4\theta_e}| \begin{bmatrix} \sin(-\omega_c t - 4\theta_e - \theta_{err,4}) \\ \cos(-\omega_c t - 4\theta_e - \theta_{err,4}) \end{bmatrix}$$

$$+ |I_{\Delta L1\_8\theta_e}| \begin{bmatrix} \sin(-\omega_c t + 8\theta_e + \theta_{err,8}) \\ \cos(-\omega_c t + 8\theta_e + \theta_{err,8}) \end{bmatrix} \quad (13)$$

where

$$|I_{\sum L}| = \frac{v_c}{\omega_c} \frac{\sum L}{\sum L^2 - \Delta L^2 - L_{dq}^2} \begin{bmatrix} \sin(\omega_c t) \\ \cos(\omega_c t) \end{bmatrix}$$

$$|I_{\Delta L}| = \frac{v_c}{\omega_c} \frac{\sqrt{\Delta L^2 + L_{dq}^2}}{\sum L^2 - \Delta L^2 - L_{dq}^2}$$

$$|I_{\Delta L1\_-4\theta_e}|$$
$$= \frac{v_c}{\omega_c} \frac{\sqrt{\Delta L_1^2 + L_{dq,1}^2 + 2\Delta L_1 L_{dq,1} \cos(\theta_{\Delta 1} - \theta_{dq,1})}}{2(\sum L^2 - \Delta L^2 - L_{dq,1}^2)}$$

$$|I_{\Delta L1\_8\theta_e}|$$
$$= \frac{v_c}{\omega_c} \frac{\sqrt{\Delta L_1^2 + L_{dq,1}^2 - 2\Delta L_1 L_{dq,1} \cos(\theta_{\Delta 1} - \theta_{dq,1})}}{2(\sum L^2 - \Delta L^2 - L_{dq,1}^2)}$$

$$\theta_{err,4} = \tan^{-1} \left[\frac{\Delta L_1 \sin \theta_{\Delta 1} + L_{dq,1} \sin \theta_{dq,1}}{\Delta L_1 \cos \theta_{\Delta 1} - L_{dq,1} \cos \theta_{dq,1}} \right]$$

$$\theta_{err,8} = \tan^{-1} \left[\frac{\Delta L_1 \sin \theta_{\Delta 1} - L_{dq,1} \sin \theta_{dq,1}}{\Delta L_1 \cos \theta_{\Delta 1} + L_{dq,1} \cos \theta_{dq,1}} \right]$$

As seen from $\mathbf{I}_{\alpha\beta G\_HF}$ in (13), the inductance harmonic $h' = 1$ causes both 4th- and 8th-order HF current harmonics where their magnitudes are respectively denoted by $|I_{\Delta L1\_-4\theta_e}|$ and $|I_{\Delta L1\_8\theta_e}|$. Because the fundamental HF current harmonic is located at $2\theta_e$, these two current harmonics cause 6th-order periodic harmonics with different position offsets $\theta_{err,4}$ and $\theta_{err,8}$ on the position estimation. It is noteworthy that the saliency-based position estimation is primarily based on the tracking of $2\theta_e$ spatial signal in (13). If secondary current harmonic of either $|I_{\Delta L1\_-4\theta_e}|$ or $|I_{\Delta L1\_8\theta_e}|$ is higher than $2\theta_e$ current $|I_{\Delta L}|$, the position estimation ultimately fails. More importantly, these secondary harmonics are primarily caused by the saturation. Thus, their magnitudes increase as the load increase.

Fig. 4 demonstrates the saliency image $i_{\beta G\_HF}$ versus $i_{\alpha G\_HF}$ considering the influence of secondary current harmonic, $h' = 1$ based on (13). In this simulation, two ratios of $\Delta L_1/\Delta L = 0.3$ and $\Delta L_1/\Delta L = 1.3$ are compared in Fig. 4(a) and (b). The mutual inductance $L_{dq,1}$ is assumed as zero for simplicity. As shown in Fig. 4, both the ellipse size and orientation change as rotor rotates. Different from saliency images in Fig. 2, the minor-axis is no longer simply aligned with the instantaneously rotor position. For example,
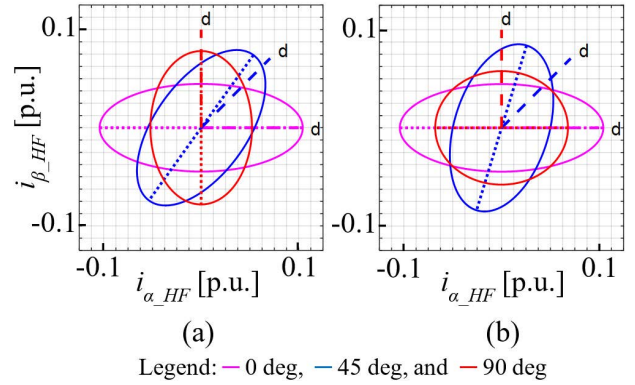

(a)   (b)

Legend: — 0 deg, — 45 deg, and — 90 deg

FIGURE 4. HF current trajectory of $i_{\beta G\_HF}$ versus the $i_{\alpha G\_HF}$ at different rotor positions where the secondary over fundamental inductance harmonic ratio is (a) (a) $\Delta L1/\Delta L = 0.3$ and (b) $\Delta L1/\Delta L = 1.3$.

(a)   (b)

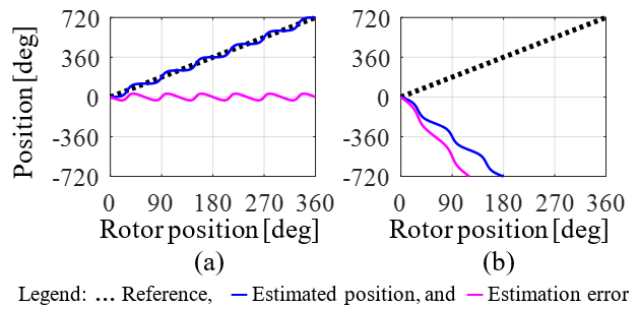Legend: ... Reference, — Estimated position, and — Estimation error

FIGURE 5. Comparison of saliency-based position estimation with the secondary inductance harmonic where the secondary over fundamental harmonic ratio is (a) $\Delta L1/\Delta L = 0.3$ and (b) $\Delta L1/\Delta L = 1.3$.

minor-axis in (b) at 0, 45, and 90 deg is not aligned with corresponding positions. Under this effect, pulsating errors occur on the position estimation. More importantly once secondary harmonic magnitudes are higher than $2\theta_e$ harmonic whereby $\Delta L_1/\Delta L = 1.3$ in Fig. 4(b), the ellipse size results in the visible change and the axis is no longer aligned with the rotor position, leading to the infeasible estimation. Fig. 5 further evaluates the saliency-based position estimation under the influence of secondary harmonic similar to Fig. 4, $\Delta L_1/\Delta L = 0.3$ and $\Delta L_1/\Delta L = 1.3$.

In this simulation, a synchronous reference frame filter in [7] is implemented to isolate position dependent signals in $i_{\alpha G\_HF}$ and $i_{\beta G\_HF}$. After that, the arctangent calculation is used to realize the position estimation. In Fig. 5(a), 6th-order position harmonic is observed because of the secondary harmonic in (13). More important in Fig. 5(b) once secondary harmonic is larger than fundamental, the position estimation eventually fails. This result is consistent with the analysis in (13). Secondary inductance harmonics are key issues to limit the position estimation. The infeasible estimation is resultant once the resulting secondary current harmonics are higher than the fundamental saliency current.

III. FEA SIMULATION

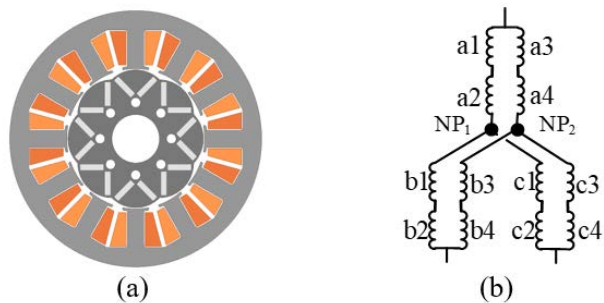A 6 kW IPM machine prototype is built for FEA simulation to verify the influence of saturated and non-sinusoidal

FIGURE 6. Illustration of test PM machine: (a) stator/rotor topology, and (b) windings configuration.

TABLE 1. Tested PM machine characteristics.

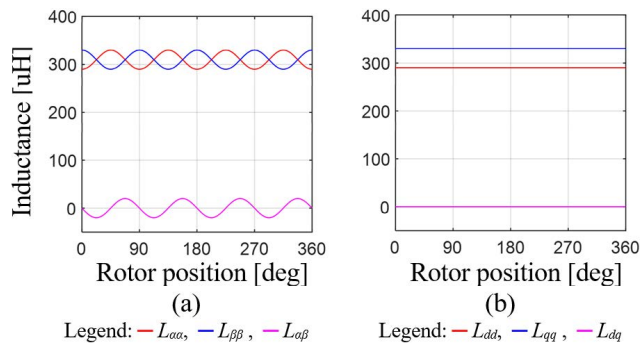| Characteristics	Values
Rotor poles	8
Stator slots	12
Rated torque	19.5 Nm
Rated current	105 A
Rated speed	3000 rpm (200 Hz elec. frequency)
Resistance	0.03 Ω/phase
Inductance	0.33/0.30 mH (L_{qq}/L_{dd})
DC bus voltage	90 V

FIGURE 7. Simulation of d-q and α-β frame self- and mutual-inductances for the test machine: d-q inductances at (a) no load and (b) full load, and α-β inductances at (c) no load and (d) full load.

inductance on the saliency-based position estimation. Key machine and drive specification are listed in Table 1. The geometric feature of test machine is shown in Fig. 6. It contains an 8-pole rotor with V-shape topology and a 12-slots concentrated windings.

A. INDUCTANCE WAVEFORM DISTORTION
The inductance waveforms versus various load conditions are analyzed in this section. The test machine model with linear magnetic materials is firstly investigated in Fig. 7. For the d-q frame self-inductance and mutual-inductance in Fig. 7(b), L_{dd} and L_{qq} are constant values and the mutual-inductance L_{dq} is zero.

Besides for α-β frame self-inductances and mutual-inductance in Fig. 7(a), $L_{\alpha\alpha}$, $L_{\beta\beta}$, and $L_{\alpha\beta}$ all results in
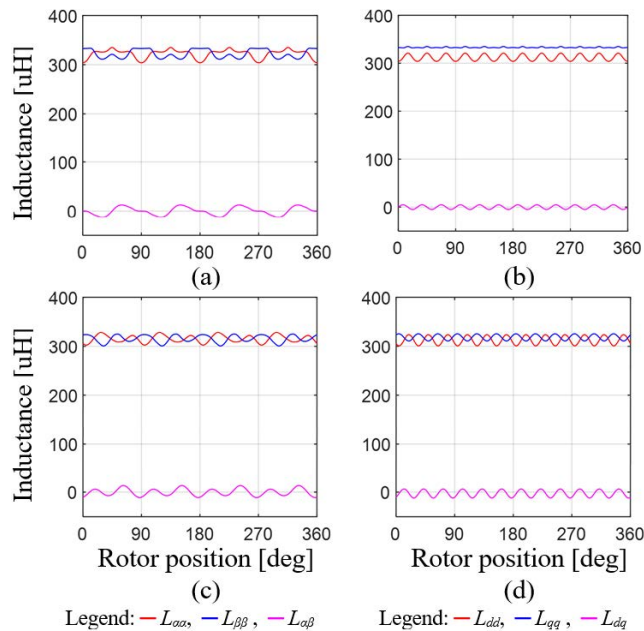

FIGURE 8. Simulation of d-q and α-β frame self- and mutual-inductances for the test machine with nonlinear magnetic materials: α-β inductances at (a) no load and (b) full load, and d-q inductances at (c) no load and (d) full load.

sinusoidal waveforms. These waveforms are similar to the ideal inductance waveforms.

The machine model considering nonlinear magnetic materials is then compared. Fig. 8(b) and (d) illustrate the *d-q* frame self-inductances L_{dd} and L_{qq}, as well as the mutual-inductance L_{dq} at no-load and full-load conditions. Besides, Fig. 8(a) and (c) shows the corresponding α-β frame self-inductances $L_{\alpha\alpha}$ and $L_{\beta\beta}$, and mutual-inductances $L_{\alpha\beta}$. Based on FEA, the non-linear inductance saturation could be considered at different loads. Different from Fig. 7(b) even at no-load condition, L_{dd} in Fig. 8(b) contains visible 6th-order harmonic because of the inductance distortion. The harmonic with 6th-order is consistent with the inductance model derived in (10). More importantly at full load, L_{qq} significantly reduces where the magnitude is almost the same as L_{dd}. In addition, the mutual-inductance L_{dq} contains both constant offset and 6th-order harmonic. These non-ideal attributes are primarily caused by the saturation. Both the constant offset and harmonic increase as load increases. On the other hand, Fig. 8(c) and (d) illustrate the corresponding α-β frame inductances. Because of the saturation, all inductances distort from ideal sinusoidal waveforms. For the saturated inductance model in Fig. 1, $K_{\Sigma sat}$ and $K_{\Delta sat}$ both equal unit value can be assumed at no-load condition in Fig. 8(b). In this case at full-load condition in Fig. 8(d), the corresponding $K_{\Sigma sat}$ and $K_{\Delta sat}$ are respectively 0.9889 and 0.2320. More importantly, the peak value in $L_{\alpha\alpha}$ is at 60 deg instead of 90 deg from the ideal model in Fig. 1. Under this effect, the position estimation eventually fails under load due to the saturation reflected position offset and harmonics.
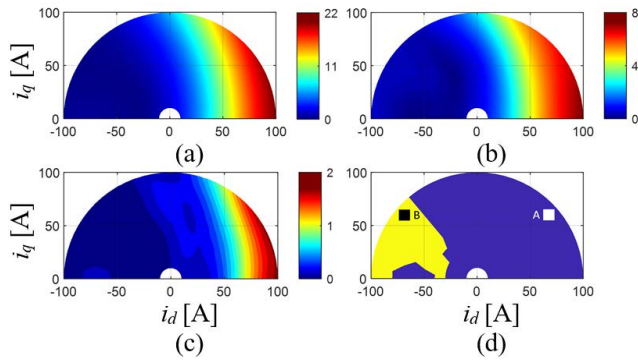
FIGURE 9. Saliency current contour versus d-axis and q-axis current, where (a) $2\theta_e$ harmonic induced current [mA], (b) secondary $4\theta_e$ harmonics induced current [mA], (c) secondary $8\theta_e$ harmonics induced current [mA] and (d) feasible position estimation region (blue) and infeasible region (yellow) for the test machine.
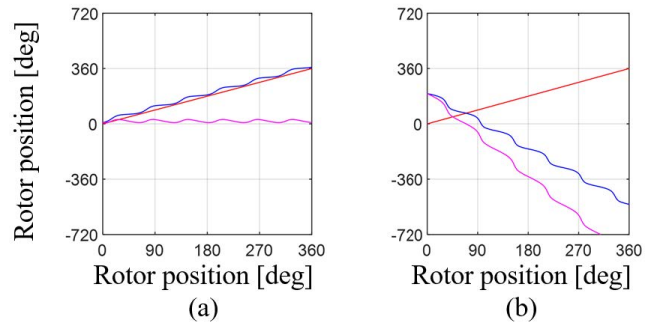
B. INFEASIBLE POSITION ESTIMATION REGION

This part investigates the infeasible estimation region. As mentioned in section II part C, secondary inductance harmonics cause additional current harmonics, as derived in (14). Once any secondary current harmonic magnitude, e.g. $|I_{\Delta L1\_-4\theta_e}|$ or $|I_{\Delta L1\_8\theta_e}|$, is higher than the fundamental current magnitude $|I_{\Delta L}|$, the position estimation causes considerable errors, and eventually leads to the infeasible estimation.

Fig. 9 analyzes saliency current magnitudes contour caused by different inductance harmonics versus q-axis current i_q and d-axis current i_q. In Fig. 9, the motor inductance is simulated using ANSYS FEA software for the saliency current analysis. The HF voltage $V_{\alpha\beta\_HF}$ in (5) is designed to be 1V with 1kHz injection frequency. The rotor speed is 1rpm to manipulate the low speed operation. In Fig. 9(a), the main $2\theta_e$ saliency current harmonic magnitude $|I_{\Delta L}|$ is analyzed at different load conditions. It is observed that $|I_{\Delta L}|$ results in the insufficient magnitude when negative i_d is applied. In general, L_{dd} increases while L_{qq} decreases once $-i_d/+i_q$ is applied for typical MTPA control. By contrast, secondary saliency current harmonics induced by $4\theta_e$ and $8\theta_e$ are respectively illustrated in Fig. 9(b) and (c). Once either the $4\theta_e$ or $8\theta_e$ secondary current harmonic magnitude is higher than the $2\theta_e$ magnitude, the position estimation ultimately fails. This infeasible estimation typically occurs when $-i_d$ is higher than a certain value. By comparing these current magnitudes, Fig. 9(d) indicates the infeasible region for the saliency-based position estimation. In this figure, the infeasible region is defined when the operation point is located under (14).

$$|I_{\Delta L}| < |I_{\Delta L1\_-4\theta_e}| \ or \ |I_{\Delta L}| < |I_{\Delta L1\_8\theta_e}|$$
$$2\theta_e \ magnitude < 4\theta_e \ or \ 8\theta_e \ harmonic \ magnitude \quad (14)$$

Fig. 10 analyzes the position estimation performance under different current loads. In this figure, the position is directly calculated through the arctangent calculation of i_{α_HF} and i_{β_HF} in (13). Both i_{α_HF} and i_{β_HF} are calculated based on the nonlinear inductance data under various loads using FEA.

FIGURE 10. Saliency-based position estimation for different operating points: (a) point A and (b) point B in Fig. 9(d).

Fig. 10(a) shows the position estimation for the operating point at point A in Fig. 9(d) within the proposed feasible region. By contrast in Fig. 10(b), point B is selected inside the infeasible region. Both current loads in Fig. 10(a) and (b) are the same while only the phase angle is different.

Although a certain amount of estimation error could be observed at point A, the estimation maintains stable. More importantly, compensation methods could be implemented based on the inductance model in section II [20], [21]. However, at point B, a totally incorrect estimation that shows the opposite direction and doubled speed is observed. It is not possible to maintain the stability inside this specific region. It is noted that the estimation accuracy also decreases once the operation point is close to the infeasible region though the estimation stability is achieved.

C. INFLUENCE ON TORQUE OUTPUT

In order to analyze the influence of position estimation errors on the generated torque, the torque contour using FOC with different position feedback signals is compared in this part. They are encoder-based measured position and saliency-based position estimation. The software-in-loop co-simulation technique is applied to combined the FEA model of test motor with the inverter circuit, and FOC and position estimation algorithm.
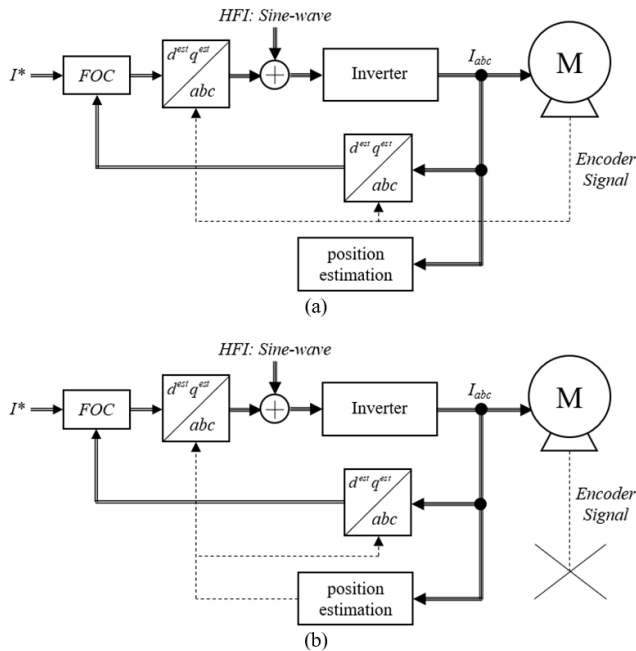
For the encoder-based drive in Fig 11(a), the FOC drive is realized based on the measured position through encoder. Fig. 12(a) demonstrates the corresponding control diagrams for MTPA control in Fig. 11(a) while the *actual* position is used for d-q transformation. In this case, the corresponding torque contour in Fig. 11(a) is illustrated in *actual d-q* reference frame. As seen in Fig. 11 (a), the maximum torque is achieved with $-i_d/i_q$ once the encoder position is implemented.

By contrast for the saliency-based drive in Fig. 11(b), the FOC drive is implemented based on the estimated position. Fig. 12(b) illustrates the corresponding signal flowchart. Different from Fig. 12(a), the estimated position is used for d-q transformation. Under this effect, the torque contour in Fig. 11(b) is shown in *estimated d-q* frame where the superscript of *est* is added to distinguish from actual frame.
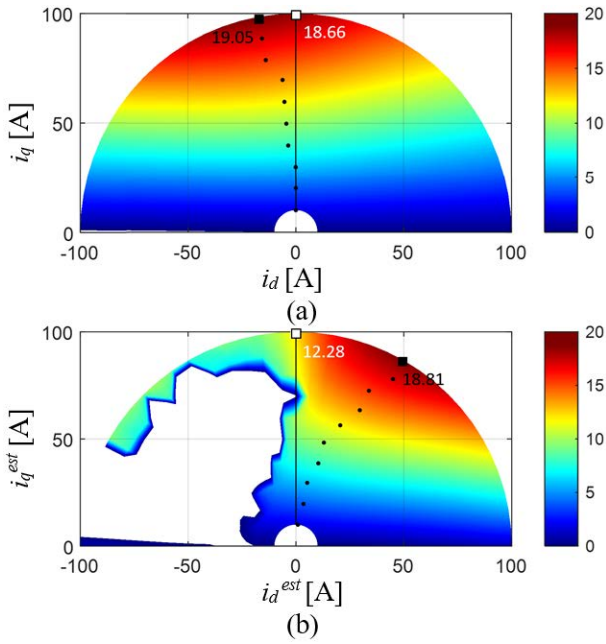
FIGURE 11. Average torque contour versus actual and estimated d- and q- current with different current regulation controls: (a) torque contour with encoder-based drive under the actual d-q current frame, (b) torque contour with saliency-based drive under the estimated d-q current frame, where the blank area in the left-hand plane represents the infeasible region where a stable control could not be realized.

FIGURE 12. Illustration of different FOC drives: (a) the encoder-based drive for MTPA torque control in Fig. 11(a), and (b) salience-based drive in Fig. 11(b).

Because of the cross-saturation and secondary harmonics mentioned in section II, position estimation errors affect the MTPA control performance. Considering these errors, a significant torque output reduction is observed at estimated

$-i_d^{est}/i_q^{est}$ point. Different from the saliency current simulation in Fig. 9, the cross-saturation is also considered in Fig. 11(b). Considering both the cross-saturation and inductance harmonics, the infeasible region in Fig. 11(b) is bigger comparing to the region in Fig. 9.

It is noted that in Fig. 11(b), the peak torque is appeared under $+i_d^{est}/i_q^{est}$ in estimated frame. From the analytical model in section II, the saliency-based position estimation errors consist of position offset θ_{offset} in (9) and position harmonics in (13). The torque output generated by the PM machine is represented by (15)

$$\mathrm{T}_e = \frac{3}{2} n_p \left[\lambda_{pm} + (L_d - L_q) i_d \right] i_q \tag{15}$$

where λ_{pm} is the PM flux and n_p is number of rotor pole pairs. However, the actual d- and q-axis current is not possible to obtain if there are errors between actual position and estimated position. In general, the relationship between actual and estimated d- and q-axis current is shown by (16).

$$\begin{bmatrix} i_d \\ i_q \end{bmatrix} = \begin{bmatrix} \cos(\theta_{err}) & \sin(\theta_{err}) \\ -\sin(\theta_{err}) & \cos(\theta_{err}) \end{bmatrix} \begin{bmatrix} i_d^{est} \\ i_q^{est} \end{bmatrix} \tag{16}$$

where θ_{err} is position errors including the position offset due to the inductance cross-saturation, and the periodic errors due to inductance harmonics. Therefore, the torque can be derived by (17) with estimated d- and q-axis current considering estimation errors.

$$\mathrm{T}_e = \frac{3}{2} n_p \left\{ \lambda_{pm} + (L_d - L_q) \left[i_q^{est} \sin(\theta_{err}) + i_d^{est} \cos(\theta_{err}) \right] \right\} \cdot \left[i_q^{est} \cos(\theta_{err}) - i_d^{est} \sin(\theta_{err}) \right] \tag{17}$$

Comparing the torque contour in Fig 11(a) and (b), the MTPA current trajectory should be redesigned for the saliency-based drive due to the effect of the *dq* cross-saturation and the secondary inductance harmonics.

IV. EXPERIMENTAL RESULTS

The same 8-pole IPM machine prototype illustrated in Fig. 6 is built for the verification of saliency-based position estimation. Fig. 13 illustrates the photograph of saliency-based test bench. The test machine is coupled to a load machine for the load operation. The inverter switching frequency is set at 10kHz synchronous to the sample frequency. All position estimation algorithms are implemented in a 32-bit microcontroller, TI-TMS320F28069.

A. INDUCTANCE MEASUREMENT

The test machine inductance is firstly tested. For the inductance measurement, the rotor is locked by the load machine. An AC voltage is applied across machine two phases through the inverter where the third phase is open. Based on this measurement, the self-inductance $L_{\beta\beta}$ can be obtained by (18).

$$V_{ab} = j\omega_c \left(L_{aa} - L_{ab} + L_{bb} - L_{ab} \right) I_{ab} = j\omega_c 2 L_{\beta\beta} I_{ab} \tag{18}$$

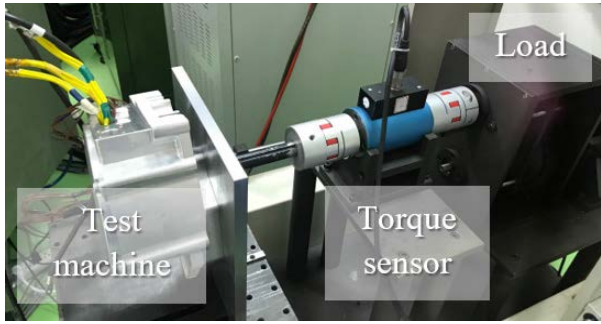where V_{ab} and I_{ab} are respectively the line voltage and current across A- and B-phase.

FIGURE 13. Test bench of PM machine saliency-based position estimation.
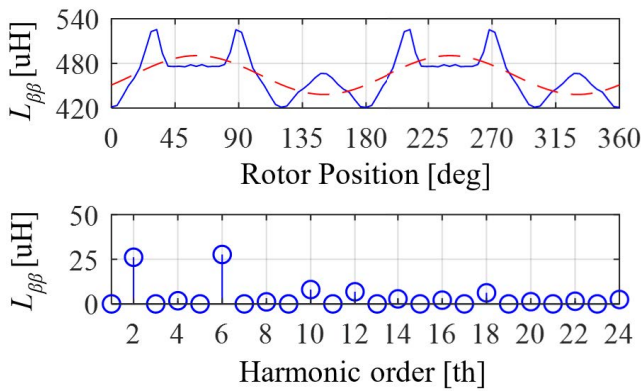

FIGURE 14. Measured self-inductance and corresponding spectrum with respect to the position (locked rotor and no load).

Fig. 14 illustrates the measured $L_{\beta\beta}$ and the spectrum of inductance harmonics. Instead of fundamental $2\theta_e$ harmonic, secondary harmonics appear at $6\theta_e$, $12\theta_e$ …etc. Among these secondary harmonics $6\theta_e$, harmonic is highest where the magnitude is around 106% with respect to $2\theta_e$ harmonic. This result is consistent with the proposed general inductance matrix $\mathbf{L}_{dq\_G}$ in (10). The 6th-order periodic harmonic on the saliency-based position estimation is expected.

B. INFEASIBLE POSITION ESTIMATION REGION

This part evaluates the saliency-based position estimation limitation at different loads. In this experiment, the test machine speed is maintained at 30 rpm through the external dyno. The saliency-based position estimation based on [22] is implemented on the test machine for MTPA control. Fig. 12(b) illustrates the corresponding FOC drive through the saliency-based position estimation. For the following experiments, no position error compensation is applied to clearly evaluate the position estimation performance. The injection voltage is 20% DC bus at 1kH frequency. The rotor position is estimated at different current conditions from 0A to 105A. Fig. 15 shows the experiment of feasible saliency-based estimation region. In this experiment, the infeasible region is defined when the position estimation has the opposite trend comparing to the actual position. In this case, no torque can be generated where the FOC is not possible. It is observed that the experimental feasible estimation region is
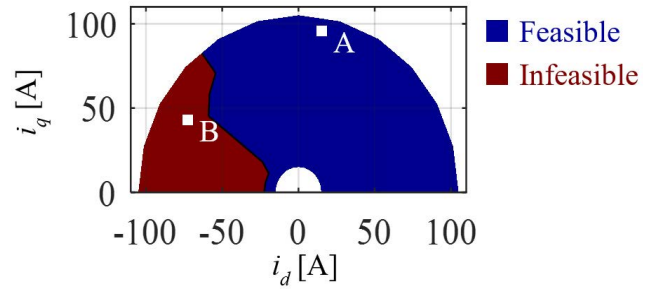

FIGURE 15. Experiment of feasible estimation region for the test IPM machine using the saliency-based sensorless drive (30 rpm).
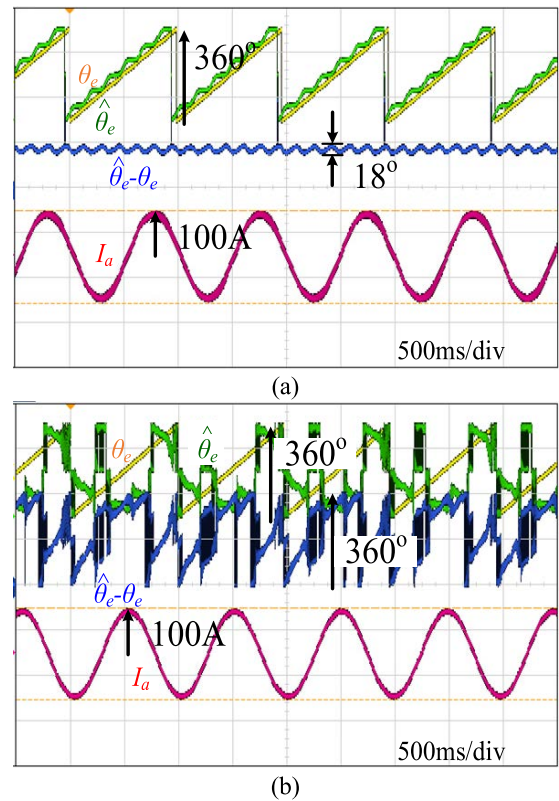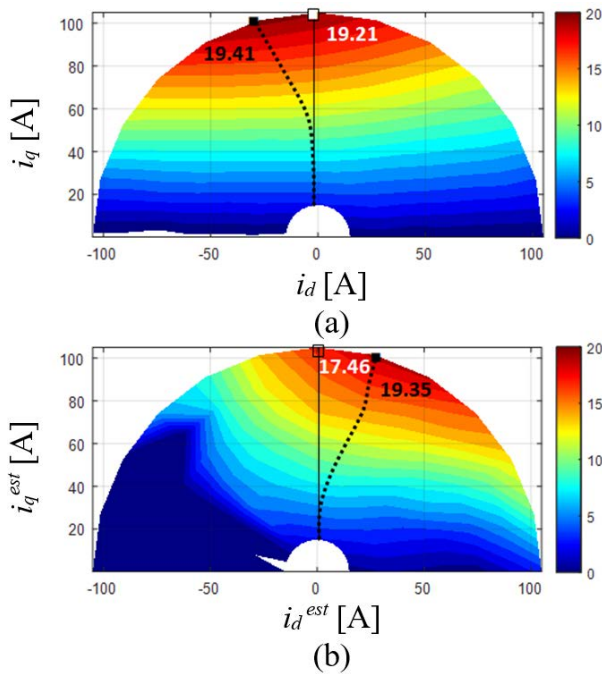

FIGURE 16. Saliency-based position estimation at two different operating points: (a) A and (b) B in Fig. 15.

similar to the predicted feasible region in Fig. 9(d). As a result, the saliency-based estimation performance can be predicted in advance based on the proposed saliency current model in (14) through the FEA of 6th-order secondary current harmonic magnitude. Fig. 16 further demonstrates the saliency-based position estimation at two representative current conditions in Fig. 16. Fig. 16(a) shows time-domain waveforms of estimated position, measured position and A-phase current for A point in Fig. 15. It is within the feasible region where the stable estimation is expected. In this point, i_d/i_q is respectively at 23.9A/86.3A. It is concluded that the saliency-based estimation maintains stable though visible 6th-order harmonic occurs. This 6th-order harmonic error is the same with the analytical prediction in Fig. 5. By contrast,

FIGURE 17. Experiment of torque [Nm] contour where the rotor position is obtained from (a) actual sensor and (b) saliency-based estimation (30 rpm rotor speed).

Fig. 16(b) shows same waveforms at B point in Fig. 15. The corresponding i_d/i_q is $-86.3A/23.9A$ within the infeasible estimation region.

Because the magnitude of secondary current harmonics is higher than the fundamental $2\theta_e$ harmonic, the saliency-based position estimation is not possible. In this case, the sensorless drive ultimately fails.

C. INFLUENCE OF INDUCTANCE HARMONICS ON TORQUE OUTPUT

The influence of non-sinusoidal inductance on the torque production is tested at this part. In this experiment, the test machine is torque controlled with current regulation where the torque is measured through a torque sensor. Fig. 17 compares the measured torque contour where the position feedback is obtained by (a) encoder sensor and (b) saliency-based position estimation. Similar to the torque simulation in Fig. 11, the torque contour under the saliency-based drive is illustrated in the estimated dq frame to clearly investigate position errors caused by the saliency-based estimation. It is expected that the peak torque is appeared under $+i_d^{est}/i_q^{est}$ in estimated frame considering the position offset θ_{offset} in (9).

For the encoder-based drive in Fig. 17(a), the maximum torque at rated current is observed where the $-i_d/i_q$ is $-35.9A/98.7A$. Based on the actual position measurement, it is consistent with the original MTPA control principle where negative id is applied to generate the reluctance torque.

However in Fig. 17(b), the estimated position is implemented for the current regulation as seen in Fig. 12(b). Under

this effect, d- and q-axis current derived from estimated position consist of both position offset and periodic position harmonics. If these position errors are unknown, visible reduction on the torque output is resultant under the same MTPA current trajectory in Fig. 17(a). In the estimated current frame, the maximum torque appears at $+i_d^{est}/i_q^{est} = 27.2A/101.4A$. Under this effect, the comparable torque with 19.5 Nm can be maintained once the saturation reflected position offset is compensated with the inductance saturation knowledge from FEA. Nevertheless, q-axis current i_q^{est} without negative d-axis current $-i_d^{est}$ is suggested to maintain MTPA control stability if the machine saturation condition is unknown.

V. CONCLUSION

The analysis of saliency-based position estimation for PM machine with non-sinusoidal inductance is proposed. The analytical model which considers inductance self-saturation, cross-saturation and secondary inductance harmonics on the position estimation is developed. The feasible region of saliency-based drive can then be predicted at different conditions. A modified MTPA current trajectory considering all estimation errors is proposed to maintain the saliency-based drive for IPM machines with saturated non-sinusoidal inductances.

REFERENCES

[1] M. Pacas, "Sensorless drives in industrial applications," *IEEE Ind. Electron. Mag.*, vol. 5, no. 2, pp. 16–23, Jun. 2011, doi: 10.1109/MIE.2011.941125.

[2] D. Raca, P. Garcia, D. D. Reigosa, F. Briz, and R. D. Lorenz, "Carrier-signal selection for sensorless control of PM synchronous machines at zero and very low speeds," *IEEE Trans. Ind. Appl.*, vol. 46, no. 1, pp. 167–178, Jan./Feb. 2010, doi: 10.1109/TIA.2009.2036551.

[3] S. Kim and S. Sul, "Sensorless control of AC motor—Where are we now?" in *Proc. Int. Conf. Electr. Mach. Syst.*, 2011, pp. 1–6, doi: 10.1109/ICEMS.2011.6073316.

[4] M. Roetzer, U. Vollmer, and R. M. Kennel, "Demodulation approach for slowly sampled sensorless field-oriented control systems enabling multiple-frequency injections," *IEEE Trans. Ind. Appl.*, vol. 54, no. 1, pp. 732–744, Jan./Feb. 2018, doi: 10.1109/TIA.2017.2757458.

[5] N. Bianchi, E. Fornasiero, and S. Bolognani, "Effect of stator and rotor saturation on sensorless rotor position detection," *IEEE Trans. Ind. Appl.*, vol. 49, no. 3, pp. 1333–1342, May/Jun. 2013, doi: 10.1109/TIA.2013.2253437.

[6] P. Guglielmi, M. Pastorelli, and A. Vagati, "Cross-saturation effects in IPM motors and related impact on sensorless control," *IEEE Trans. Ind. Appl.*, vol. 42, no. 6, pp. 1516–1522, Nov./Dec. 2006, doi: 10.1109/TIA.2006.882646.

[7] D. D. Reigosa, P. Garcia, D. Raca, F. Briz, and R. D. Lorenz, "Measurement and adaptive decoupling of cross-saturation effects and secondary saliencies in sensorless controlled IPM synchronous machines," *IEEE Trans. Ind. Appl.*, vol. 44, no. 6, pp. 1758–1767, Nov./Dec. 2008, doi: 10.1109/TIA.2008.2006335.

[8] D. Paulus, P. Landsmann, S. Kuehl, and R. Kennel, "Arbitrary injection for permanent magnet synchronous machines with multiple saliencies," in *Proc. IEEE Energy Convers. Congr. Expo.*, Sep. 2013, pp. 511–517, doi: 10.1109/ECCE.2013.6646744.

[9] I. P. Brown, G. Y. Sizov, and L. E. Brown, "Impact of rotor design on interior permanent-magnet machines with concentrated and distributed windings for signal injection-based sensorless control and power conversion," *IEEE Trans. Ind. Appl.*, vol. 52, no. 1, pp. 136–144, Jan./Feb. 2016, doi: 10.1109/TIA.2015.2464783.

[10] N. Limsuwan, T. Kato, and R. D. Lorenz, "Concurrent design of interior-permanent-magnet machines for self-sensing and power conversion," *IEEE Trans. Ind. Appl.*, vol. 48, no. 6, pp. 2157–2164, Nov./Dec. 2012, doi: 10.1109/TIA.2012.2226691.

[11] Y. Li, Z. Q. Zhu, D. Howe, C. M. Bingham, and D. A. Stone, "Improved rotor-position estimation by signal injection in brushless AC motors, accounting for cross-coupling magnetic saturation," *IEEE Trans. Ind. Appl.*, vol. 45, no. 5, pp. 1843–1850, Sep./Oct. 2009, doi: 10.1109/TIA.2009.2027518.

[12] Y.-C. Kwon, J. Lee, and S.-K. Sul, "Extending operational limit of IPMSM in signal-injection sensorless control by manipulation of convergence point," *IEEE Trans. Ind. Appl.*, vol. 55, no. 2, pp. 1574–1586, Mar./Apr. 2019, doi: 10.1109/TIA.2018.2882483.

[13] Y. Lee, Y.-C. Kwon, S.-K. Sul, N. A. Baloch, and S. Morimoto, "Compensation of position estimation error for precise position-sensorless control of IPMSM based on high-frequency pulsating voltage injection," in *Proc. IEEE Energy Convers. Congr. Expo. (ECCE)*, Oct. 2017, pp. 859–864, doi: 10.1109/ECCE.2017.8095875.

[14] X. Wang, W. Xie, G. Dajaku, R. M. Kennel, D. Gerling, and R. D. Lorenz, "Position self-sensing evaluation of novel CW-IPMSMs with an HF injection method," *IEEE Trans. Ind. Appl.*, vol. 50, no. 5, pp. 3325–3334, Sep./Oct. 2014, doi: 10.1109/TIA.2014.2311507.

[15] M. Barcaro, M. Morandin, T. Pradella, N. Bianchi, and I. Furlan, "Iron saturation impact on high-frequency sensorless control of synchronous permanent-magnet motor," *IEEE Trans. Ind. Appl.*, vol. 53, no. 6, pp. 5470–5478, Nov./Dec. 2017, doi: 10.1109/TIA.2017.2731298.

[16] K.-Y. Hung, N.-W. Liu, and S.-C. Yang, "Analysis of saliency-based position estimation for permanent magnet machine with saturation reflected non-sinusoidal inductance," in *Proc. IEEE 4th Int. Future Energy Electron. Conf. (IFEEC)*, Nov. 2019, pp. 1–7, doi: 10.1109/IFEEC47410.2019.9014659.

[17] P. Garcia, F. Briz, D. Raca, and R. D. Lorenz, "Saliency-tracking-based sensorless control of AC machines using structured neural networks," *IEEE Trans. Ind. Appl.*, vol. 43, no. 1, pp. 77–86, Jan./Feb. 2007, doi: 10.1109/TIA.2006.887309.

[18] Z. Chen, F. Wang, G. Luo, Z. Zhang, and R. Kennel, "Secondary saliency tracking-based sensorless control for concentrated winding SPMSM," *IEEE Trans. Ind. Informat.*, vol. 12, no. 1, pp. 201–210, Feb. 2016, doi: 10.1109/TII.2015.2503639.

[19] P. L. Xu and Z. Q. Zhu, "Comparison of carrier signal injection methods for sensorless control of PMSM drives," in *Proc. IEEE Energy Convers. Congr. Expo. (ECCE)*, Sep. 2015, pp. 5616–5623, doi: 10.1109/ECCE.2015.7310450.

[20] E. R. Montero, M. Vogelsberger, F. Baumgartner, and T. Wolbank, "Robust signal offset identification for sensorless control of induction machines at rated load using one-active modulating pulse excitation," in *Proc. IEEE Energy Convers. Congr. Expo. (ECCE)*, Sep. 2019, pp. 1867–1872, doi: 10.1109/ECCE.2019.8913040.

[21] Z. Chen, C. Wu, R. Qi, G. Luo, and R. Kennel, "Decoupling of secondary saliencies in sensorless AC drives using repetitive control," in *Proc. 17th Eur. Conf. Power Electron. Appl. (EPE ECCE-Europe)*, Sep. 2015, pp. 1–10, doi: 10.1109/EPE.2015.7309173.

[22] S.-I. Kim, J.-H. Im, E.-Y. Song, and R.-Y. Kim, "A new rotor position estimation method of IPMSM using all-pass filter on high-frequency rotating voltage signal injection," *IEEE Trans. Ind. Electron.*, vol. 63, no. 10, pp. 6499–6509, Oct. 2016, doi: 10.1109/TIE.2016.2592464.

PO-HUAN CHOU was born in Taipei, Taiwan, in 1982. He received the B.S. degree in electrical engineering from Feng Chia University, Taiwan, in 2005, and the M.S. and Ph.D. degrees in electrical engineering from the National Dong Hwa University, Taiwan, in 2007 and 2011, respectively. He is currently working with the Industrial Technology Research Institute. His research interests include servo drive systems, intelligent control, DSP-based control systems, and motion control.
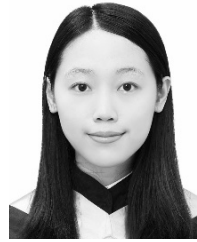
NAI-WEN LIU (Student Member, IEEE) received the M.S. degree in electrical engineering from the National Sun Yat-sen University, Kaohsiung, Taiwan, in 2016. She is currently pursuing the Ph.D. degree in mechanical engineering with the National Taiwan University, Taipei, Taiwan. Her main research interests include drive and control systems development, finite-element analysis of motor design, and the electromagnetic characteristics and performance with the drive circuit.

YU-LIANG HSU (Member, IEEE) received the B.S. degree in automatic control engineering from Feng Chia University, Taichung, Taiwan, in 2004, and the M.S. and Ph.D. degrees in electrical engineering from the National Cheng Kung University, Tainan, Taiwan, in 2007 and 2011, respectively. He is currently an Assistant Professor with the Department of Mechanical and Electro-Mechanical Engineering, National Sun Yat-sen University, Taiwan. His research interests include computational intelligence, human–robot interaction, biomedical engineering, nonlinear system identification, and wearable intelligent technology. He has been a member of the Phi Tau Phi Honor Society, since 2004. He received the Best Paper Award of 2012 Conference on ISG*ISARC, the Merit Paper Award of TAAI 2013, the First Prize Paper Award of IEEE ICASI 2017, the Best Conference Paper Award of IEEE ICASI 2018, and the Best Conference Paper Award of IEEE ECBIOS 2021.

KUO-YUAN HUNG (Student Member, IEEE) received the M.S. degree in electrical engineering from the National Sun Yat-sen University, Kaohsiung, Taiwan, in 2015. He is currently pursuing the Ph.D. degree in mechanical engineering with the National Taiwan University, Taipei, Taiwan. His research project focuses on the motor electromagnetic characteristics by using finite element analysis, the motor prototype, drive controller, and model the mathematical model of the motor. He is specialized in coupling simulation control architecture analysis, mainly using the saliency effect of the motor inductance to build a position sensorless control system.

SHIH-CHIN YANG (Senior Member, IEEE) was born in Taiwan. He received the M.S. degree from the National Taiwan University, Taiwan, in 2007, and the Ph.D. degree from the University of Wisconsin–Madison, Madison, WI, USA, in 2011.

From 2011 to 2015, he was a Research Engineer with Texas Instruments Motor Laboratory, Dallas, TX, USA. He is currently a Professor with the National Taiwan University, with the responsibility on the development of motor drive and motor control technology. He is also the Nidec Adjunct Professor collaborated with various industrial and automobile motor business units worldwide. He was a recipient of two conference paper awards from IEEE Energy Conversion Congress and Exposition. He is the Publications Chair of the 2021 IEEE International Future Energy Electronics Conference. He is an Associate Editor of the IEEE TRANSACTIONS ON POWER ELECTRONICS. He is an Invited Speaker on 2020 IEEE PELS Day and 2018 S2PC.

• • •